

# Open Research Online

---

The Open University's repository of research publications and other research outputs

## The influence of electron multiplication and internal X-ray fluorescence on the performance of a scintillator-based gamma camera

### Journal Item

How to cite:

Hall, David; Holland, Andrew and Soman, Matthew (2012). The influence of electron multiplication and internal X-ray fluorescence on the performance of a scintillator-based gamma camera. *Nuclear Instruments and Methods in Physics Research Section A: Accelerators, Spectrometers, Detectors and Associated Equipment*, 678 64- 77.

For guidance on citations see [FAQs](#).

© 2012 Elsevier B.V.

Version: Accepted Manuscript

Link(s) to article on publisher's website:  
<http://dx.doi.org/doi:10.1016/j.nima.2012.03.013>

---

Copyright and Moral Rights for the articles on this site are retained by the individual authors and/or other copyright owners. For more information on Open Research Online's data [policy](#) on reuse of materials please consult the policies page.

---

[oro.open.ac.uk](http://oro.open.ac.uk)

# The influence of electron multiplication and internal X-ray fluorescence on the performance of a scintillator-based gamma camera

David J. Hall<sup>a,\*</sup> Andrew Holland<sup>a</sup> Matthew Soman<sup>a</sup>

<sup>a</sup>*e2v centre for electronic imaging, The Open University,  
Walton Hall, Milton Keynes MK7 6AA, UK*

---

## Abstract

When considering the ‘standard’ gamma-camera, one might picture an array of photo-multiplier tubes or a similar array of small-area detectors. This array of imaging detectors would be attached to a corresponding array of scintillator modules (or a solid layer of scintillator) in order to give a high detection efficiency in the energy region of interest, usually 8-140 keV. Over recent years, developments of gamma-cameras capable of achieving much higher spatial resolutions have led to a new range of systems based on Charge-Coupled Devices with some form of signal multiplication between the scintillator and the CCD in order for one to distinguish the light output from the scintillator above the CCD noise. The use of an Electron-Multiplying Charge-Coupled Device (EM-CCD) incorporates the gain process within the CCD through a form of ‘impact ionisation’, however, the gain process introduces an ‘excess noise factor’ due to the probabilistic nature of impact ionisation and this additional noise consequently has an impact on the spatial and spectral resolution of the detector. Internal fluorescence in the scintillator, producing K-shell X-ray fluorescence photons that can be detected alongside the incident gamma-rays, also has a major impact on the imaging capabilities of gamma-cameras. This impact varies dramatically from the low spatial resolution to high spatial resolution camera system. Through a process of simulation and experimental testing focussed on the high spatial resolution (EM-CCD based) variant, the factors affecting the performance of gamma-camera systems are discussed and the results lead to important conclusions to be considered for the development of future systems. This paper presents a study into the influence of the EM-CCD gain process and the internal X-ray fluorescence in the scintillator on the performance of scintillator-based gamma cameras (CCD-based or otherwise), making use of Monte Carlo simulations to demonstrate the aspects involved, their influence on the imaging system and the hypotheses previously discussed in experimental studies.

*Key words:* Gamma camera, CCD, EM-CCD, scintillator, resolution, fluorescence

---

# 1 Introduction

2 There are many applications for gamma-cameras in the energy regime from  
3 8-140 keV, from medical imaging to synchrotron-based research. It is gener-  
4 ally possible to split current gamma-camera technology into two groups: low  
5 spatial resolution and high spatial resolution systems. Here, low-resolution  
6 gamma-cameras are defined as those with a resolution of a few hundred mi-  
7 crometers or greater. High-resolution gamma-cameras are defined here as those  
8 with a resolution of better than 100  $\mu\text{m}$ . The grouping occurs in this way due  
9 to the technologies behind the detectors available for such camera systems.  
10 Gamma-cameras can be made from arrays of imaging detectors, each detector  
11 creating a ‘single pixel’ and generally measuring a few hundred micrometers  
12 across. Such camera systems generally have lower resolutions in the spatial  
13 regime but comparatively better spectral resolutions [1]. Alternatively, one  
14 can manufacture a high-resolution gamma-camera from a single imaging de-  
15 vice for which each pixel is a few tens of micrometers in size [2]. Although  
16 such detector systems can have much higher spatial resolutions, the spectral  
17 resolution generally suffers (Sections 3 and 4).

18 In order to create the highest-resolution gamma-cameras, sub-pixel imaging  
19 is required and can be achieved through photon-counting imaging techniques  
20 and centroiding. The low numbers of photons recorded per event when using  
21 photon-counting techniques can be lost beneath the readout noise floor of a  
22 standard Charge-Coupled Device (CCD). If one uses an Electron-Multiplying  
23 Charge-Coupled Device (EM-CCD), then the effective readout noise can be  
24 reduced to the sub-electron level, dramatically increasing the effective signal-  
25 to-noise level. However, the gain process (‘impact ionisation’) required to in-  
26 crease the effective signal-to-noise ratio introduces an additional noise factor,  
27 the so called ‘gain noise’. This additional noise factor acts to reduce the spec-  
28 tral resolution and can be studied analytically, but the effect of the additional  
29 noise on the centroiding accuracy is more complex and hence a simulation  
30 has been produced to ascertain the level of impact of the gain process on the  
31 ability to achieve sub-pixel imaging in comparison to a similar CCD system  
32 to allow a spatial imaging performance comparison to be made.

33 When using a silicon-based detector for gamma-ray imaging, it is generally  
34 preferential to increase the detection efficiency through the use of a scintillator,  
35 either directly coupled to the detector or through a fibre-optic system. With  
36 a scintillator based detection system, experimental results suggest the K-shell  
37 fluorescence X-rays that can be generated in the scintillator from the incident  
38 gamma-rays (provided they are of energy greater than the K-shell binding

---

\* Corresponding author.

*Email address:* d.j.hall@open.ac.uk (David J. Hall).

energy) can be reabsorbed at another location in the scintillator, acting to decrease the spatial resolution of the system. Although thresholding can be used to a certain extent, this brings a dramatic reduction in the detection efficiency as, for the example of the scintillator CsI(Tl), approximately 90% of ‘true’ events can be rejected. Using a series of new simulations, validated against previously reported experimental results [2–5], to look at both the spatial and spectral capabilities of the detector systems, the impact on the resolutions of the internal fluorescence is explored for both ‘high’ and ‘low’ resolution gamma cameras.

This work develops on theory and experimental results taken from [2–5] and the PhD thesis by the author [6], with the theory in Sections 2 and 5 taken from this work. Through new additional simulations and analysis this study aims to confirm the hypotheses presented in the previous experimental work and to place the results in a wider context, developing the scope to include limitations on the camera system. For every application of the gamma-camera the desired specifications may change. Through consideration of the systems as a whole, taking into account, for example, the limitations on the spatial resolution due to the use of a collimator, the choice of system can be considered. The first choice to be made is between that of a spatially or spectrally preferential system. The choice of one detector over another is discussed and possible improvements to the detector systems inferred.

## 2 The scintillation process

Scintillators have been dominant in the field of ionising radiation detection for over one hundred years. Solid scintillation was first observed by Elster and Geitel in 1903, where the presence of an alpha-emitting source led to individual light flashes in a ZnS screen [7]. Over the last century, developments in the understanding of the scintillation process and the discovery of new scintillating materials has led to many new uses throughout high-energy physics and astrophysics, along with the continual development for medical imaging applications from the first X-ray film through to modern dental CCD imagers.

A scintillator converts the energy from the absorption of ionising radiation into a flash of photons of a much longer wavelength, usually in the visible region of the electromagnetic spectrum. In the case of the gamma-ray detection, the combination of the larger number of output photons compared to the incident flux and the lower energy of the photons produced means that scintillators are a near ideal choice for coupling to a silicon based imager (such as a CCD or CMOS device). As most higher energy X-rays will pass straight through the silicon of the device (with no scintillator present) the detection efficiency for high energy photons is much reduced. Through the inclusion of a thicker

78 scintillating layer, the detection efficiency can be greatly increased.

## 79 2.1 Inorganic scintillators

80 The scintillator acts to convert a single high-energy quantum into many lower  
81 energy quanta. The reduction in energy of the quanta to be detected leads to  
82 a much higher efficiency of detection than would be possible with the higher  
83 energy quantum.

84 The scintillation process can be described in five stages as detailed in [8]:

- 85 (1) Creation of electron-hole pairs through the absorption of ionising radia-  
86 tion.
- 87 (2) Relaxation of primary e-h pairs, producing multiple secondary electrons,  
88 holes, photons, phonons and other electronic excitations.
- 89 (3) Thermalisation of secondary e-h pairs through interactions with the vi-  
90 brations of the environment.
- 91 (4) Energy transfer to the luminescence centres.
- 92 (5) Emission of energy from luminescence centres in the form of lower energy  
93 photons.

94 At the energies considered in this study, the photo-electric effect dominates due  
95 to a larger interaction cross-section than the Compton interactions, Figure 1.  
96 Through the photoelectric effect, a hole is created in the inner electron shell of  
97 the atom (K-shell). This leaves an ionised atom and a free electron with energy  
98 equal to  $h\nu$  minus the binding energy of the electron. The ionised atom in the  
99 lattice may relax through the emission of a photon, as another electron drops to  
100 fill the hole, or through the Auger effect, where further electrons are released.  
101 The electrons then lose energy through further scattering or the emission of  
102 photons. This process continues until ionisation is no longer possible. Electrons  
103 lose excess energy through inelastic scattering until only low energy excitations  
104 in the lattice remain.

105 When the energy of the excited electrons is below the ionisation threshold,  
106 the electrons begin to interact with vibrations in the environment: the process  
107 of thermalisation. The holes move to the top of the valence band, whilst the  
108 electrons move to the bottom of the conduction band, leaving many electron-  
109 hole pairs each separated by the band gap energy  $E_g$ . This stage leaves  $N_{eh}$   
110 electron-hole pairs, Equation 1, where  $\varepsilon$  is the average energy required to create  
111 a single electron-hole pair and  $E_\gamma$  is the energy of the incident absorbed photon  
112 [8].

$$113 \quad N_{eh} = \frac{E_\gamma}{\varepsilon} \quad (1)$$

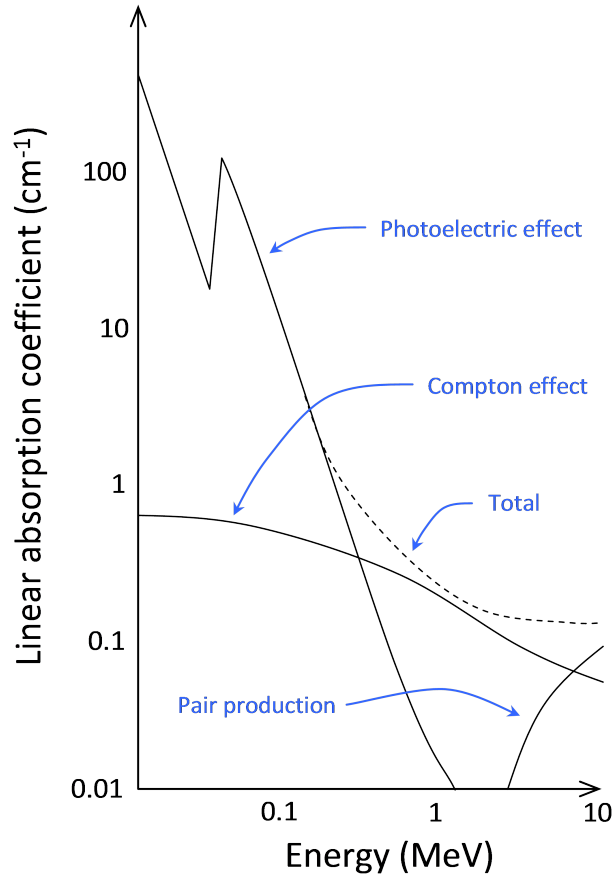


Fig. 1. The linear absorption coefficient for CsI(Tl) against incident gamma-ray energy. The photo-electric effect dominates in the region of interest in this study (below 200 keV).

114 The electronic excitations then transfer their energy to the luminescence cen-  
 115 tres in the scintillator (such as the  $Tl^+$  ions in CsI(Tl) that are involved in the  
 116 electronic recombination). The luminescence centres can be excited through  
 117 either the consecutive capture of an electron then a hole (hole recombina-  
 118 tion luminescence) or a hole then an electron (electron recombination lumi-  
 119 nescence) [8]. The emission of photons follows the relaxation of the excited  
 120 luminescence centres to their ground state.

## 121 2.2 Thallium-doped caesium iodide

122 Thallium doped Caesium Iodide is a popular scintillator choice for current  
 123 gamma-cameras due to the high emission yield (54 photons per keV gamma),  
 124 the similar refractive index to that of glass in a fibre-optic plate (1.79 at emis-  
 125 sion maximum) and the low self-absorbance (re-absorbance of emitted pho-  
 126 tons) for the slow component ( $3.4 \pm 0.5 \mu s$ ), despite the higher self-absorbance  
 127 of the fast component ( $600 \pm 50 ns$ ), although this will depend on the crystal

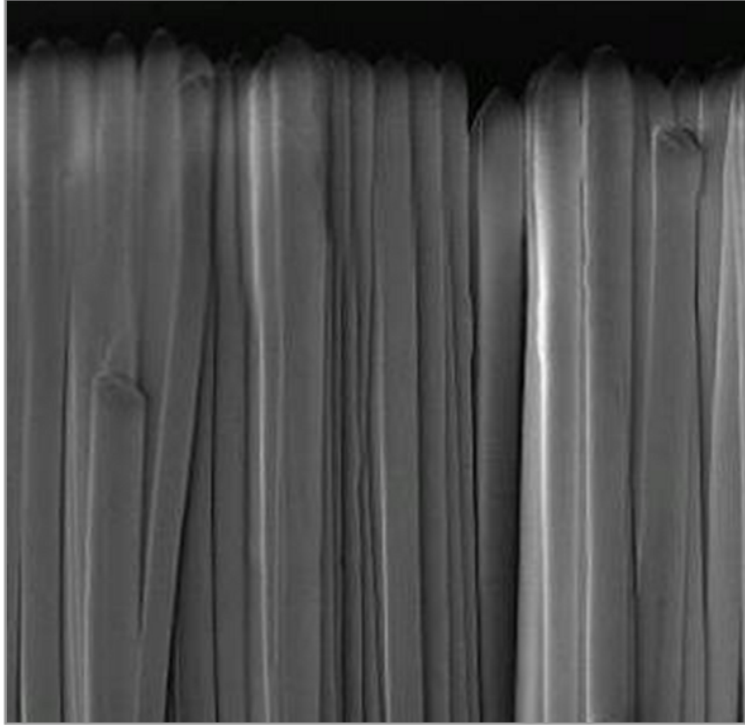


Fig. 2. An SEM of the scintillator CsI(Tl). The scintillator can be seen to be formed of columns of diameter 5-6  $\mu\text{m}$ . The sample used in this study was produced by e2v technologies with a thickness of 70  $\mu\text{m}$  [11].

128 dimensions [9,10]. The scintillator can also be grown in a columnar form that,  
129 although not perfect, reduces the spread in the light emitted in the scintilla-  
130 tor, Figure 2. In a similar way to a fibre-optic plate, the scintillator acts to  
131 channel the light to the CCD along the columnar structures, acting to reduce  
132 the light spread and increase the peak in intensity of the Gaussian-like profile  
133 observed at the CCD surface.

134 The scintillator produces approximately 60 photons per keV of incident en-  
135 ergy, forming an approximately linear dependence on energy over the range  
136 of interest. Through the analysis of the number of photons emitted, it is in  
137 theory possible to relate this figure to the energy of the incident photons [4,8].

### 138 *2.3 Internal X-ray fluorescence*

139 Interactions occurring in the scintillator due to gamma-ray irradiation must  
140 be studied in greater detail in order to ascertain the imaging capabilities of a  
141 scintillator-based camera system. The interaction process inside the scintilla-  
142 tor does not simply supply a series of identical scintillation flashes all occurring  
143 at the incident gamma-ray energy. At low energies (below the binding ener-  
144 gies of elements in the scintillator) the interaction process is simplified and

145 the number of lower energy photons produced is proportional to the incident  
146 photon energy, with one reaction point for each incident quantum.

147 For caesium iodide, the scintillator used as a demonstrator in this study, the  
148 binding energies of importance are those for caesium at 35.99 keV and iodine  
149 at 33.17 keV. Incident photons of energies below approximately 30-35 keV  
150 are not of interest here as these will provide a single spectral peak. For the  
151 imaging of harder X-rays, those above approximately 30-35 keV, one has to  
152 consider the impact of K-shell fluorescence on the imaging capabilities of the  
153 system.

154 Considering the case of a  $^{241}\text{Am}$  source providing incident gamma-rays at  
155 59.5 keV, one can discuss the internal X-ray fluorescence further. Approxi-  
156 mately 90% of interactions in the caesium iodide at 59.5 keV will be due to  
157 the photo-electric effect. Of these primary interactions, the fluorescence yield  
158 is approximately 88-90%, resulting from electrons falling from higher energy  
159 levels to fill the hole left by the ejected electron [12]. In this case, the differ-  
160 ence between the interaction probability with the caesium and iodine atoms  
161 is negligible.

162 At 59.5 keV, the incident photons have sufficient energy to knock an electron  
163 from the inner shell of the caesium and iodine atoms in the scintillator, releas-  
164 ing an electron of energy equal to the incident photon energy (59.5 keV in this  
165 case) minus the binding energy of the atom (either caesium or iodine in this  
166 case). The ejected electron has insufficient energy to travel far from the initial  
167 interaction point, but may traverse several microns. Remaining excitations in  
168 the atom, along with the scintillation caused by the ejected electron, provides  
169 the flash of photons at (or very close to) the initial interaction position.

170 Following this process, approximately 10% of the relaxations of the atoms  
171 follow the Auger process. The ejected electrons will cause scintillation sur-  
172 rounding the initial interaction position and the total sum of the number of  
173 lower energy photons produced at this point will be proportional to the inci-  
174 dent photon energy.

175 The remaining 90% of relaxations result in K-shell X-ray fluorescence, where  
176 an outer shell electron falls to fill the hole left by the ejected electron, releas-  
177 ing the difference in energy in the form of a characteristic X-ray.  $K\alpha$  emission  
178 results from approximately 90% of these interactions, with the remaining 10%  
179 resulting from  $K\beta$  emission. The emitted characteristic fluorescence X-rays  
180 may travel through the scintillator and leave the material undetected. In this  
181 case, the number of lower energy photons produced relates to the energy of the  
182 emitted electron. If, however, the fluorescence X-ray interacts with the scintil-  
183 lator, a secondary interaction site will occur away from the initial interaction  
184 point, with the distance between the two interaction sites determined by the



185 probability of interaction at the energy of the fluorescence X-ray. It is this  
186 distance between the initial interaction and the secondary event that affects  
187 the imaging capabilities of the device. This process was observed in [13,14] as  
188 a “separately resolved primary interaction and the secondary K X-ray interac-  
189 tion”, giving an ‘extra’ event outside the line of a slit placed over the camera.  
190 Here we aim to determine the impact of the detection of these ‘extra’ events  
191 on the spatial and spectral resolution using simulations designed to confirm  
192 and explore the results detailed in the experimental studies and the affect the  
193 re-absorbed fluorescence on ‘high’ and ‘low’ spatial resolution gamma cameras  
194 [2,13,14].

### 195 **3 Gamma cameras based on photo-multiplier tubes**

196 Until recently, a standard gamma-camera consisted of an array of Photo-  
197 Multiplier Tubes (PMTs) coupled to a thick scintillating layer [1]. When an  
198 X-ray photon interacts in the scintillator a flash of photons is produced that  
199 can be detected as a series of voltages from the PMT array . The coincidence  
200 of signals from a sub-array of PMTs close to the interaction location allow  
201 a weighted mean position to be calculated from the relative signals between  
202 the PMTs in the sub-array. The total sum of the signal from all detectors in  
203 the PMT array is proportional to the energy deposited in the interaction of  
204 the incident photon. In the past, PMT arrays have been limited to providing  
205 intrinsic detector spatial resolutions of the order of 3-5 mm depending on the  
206 crystal type and thickness, PMT dimensions and algorithms used [1]. However,  
207 current systems are capable of sub-millimetre precision down to a suggested  
208 limit of 0.5 mm [15], although it is noted that the spatial and energy resolution  
209 depend strongly on the scintillator used and the corresponding light output,  
210 limiting the FWHM energy resolution to approximately 9-11% for NaI(Tl)  
211 [1,15].

212 Performance in such detectors varies, dependent on the scintillator used and  
213 detector arrangements. Energy resolutions of 22-24% have been reported for  
214 CsI(Tl), in comparison to an improved performance of 14% for NaI(Tl) for the  
215 same detector formulation [16], with a best case energy resolution of 10.8%  
216 FWHM achieved with NaI(Tl) [17]. Spatial resolutions were also recorded at  
217 0.6-0.9 mm and 1.16 mm respectively, reaching the sub-millimetre level, but  
218 still a long way from the sub-100  $\mu\text{m}$  levels achievable with high resolution  
219 camera systems (Section 4). Another example is that described in [18], in  
220 which a 3 mm NaI(Tl) crystal was coupled to a PMT array (“Hamamatsu  
221 H5900-00-C12, 1-inch square cross-wire readout type”) to create a small FOV  
222 gamma-camera. The spatial resolution in this case was limited to 1.5 mm,  
223 although more recent developments of this system have led to an improvement  
224 in spatial resolution to 0.75 mm at 122 keV using a 2 mm thick LaBr<sub>3</sub>(Ce)

225 scintillator [19]. The use of a scintillator with improved light output has in  
226 this case also brought improvements in the energy resolution to 8.9% and  
227 13.4% at 122 keV and 60 keV respectively. Similar results of 0.9 mm FWHM  
228 spatial resolution have been reported in [20] using a  $\text{LaBr}_3(\text{Ce})$  scintillator  
229 and position sensitive PMT.

## 230 4 CCD-based gamma cameras

231 Following from the description above of a ‘low spatial resolution’ gamma-  
232 camera, one can consider what is required to image at a much higher spatial  
233 resolution. One of the main limiting factors of the aforementioned systems is  
234 the use of an array of PMTs. The limit on the physical size of each ‘pixel’ in  
235 the PMT array provides an optimal resolution limit above which such a system  
236 could not deliver. One way of improving the spatial resolution of a ‘standard’  
237 gamma-camera is to replace the PMT array with an ‘array of detectors’ for  
238 which the individual element size is much reduced - a CCD or CMOS/hybrid  
239 based system.

240 In order to cope with applications in which a high-flux rate is required, the  
241 readout speed of the detector must be increased to enable the use of ‘photon-  
242 counting’ techniques (Section 8.1). Unfortunately, an increase in the readout  
243 speed of a CCD leads to an increase in the readout noise. This increase in  
244 readout noise would not allow the detector to distinguish low signal levels  
245 above the random fluctuations in the ‘zero-level’ of the image. Without any  
246 readout noise and no signal present (of any type) then one would expect a  
247 flat field image of zeros (a true ‘zero-level’). However, with read noise, this  
248 flat field of zeros is altered such that the ‘zero-level’ fluctuates due to the  
249 random noise measured at the output of the camera system [21]. The increase  
250 in readout noise can, however, be counteracted through the use of off-chip  
251 or on-chip amplification of the signal - increasing the signal level before the  
252 addition of the readout noise component.

253 The early development of the ‘BazookaSPECT’ system demonstrates the use  
254 of off-chip signal amplification through the use of a second generation imaging  
255 intensifier and lens system to amplify the signal from the scintillator before  
256 reaching the CCD [22,23]. In comparison with the systems described previ-  
257 ously, very high spatial resolutions can be achieved down to 50  $\mu\text{m}$ . As the  
258 name of the system suggests, however, there are physical detector system di-  
259 mension limitations that may only be overcome through the use of on-chip  
260 signal amplification.

## 261 5 On-chip signal amplification

262 The number of signal electrons in a charge packet in a CCD can be increased  
263 through the process of ‘impact ionisation’ [21]. When a controllable high volt-  
264 age is placed over a CCD electrode, creating a high electric field between this  
265 and neighbouring electrodes, the ‘impact ionisation’ process can be controlled.  
266 With an increase in the signal charge and no subsequent increase in readout  
267 noise, the ‘effective readout noise’ (compared to original signal level) can be  
268 reduced to the sub-electron level.

### 269 5.1 *The Electron-Multiplying CCD*

270 The Low-Light-Level camera uses an Electron-Multiplying CCD (EM-CCD)  
271 [24] to provide all light level imaging from bright sunlight down to shadowed  
272 overcast starlight. The variable gain allows the device to be run as a standard  
273 CCD in sunlight with unity gain and also down to very low light levels by  
274 increasing the gain level. The multiplication of the signal before readout ef-  
275 fectively reduces the readout noise which can be reduced to the sub-electron  
276 level [25]. The very low readout noise allows the detection of signals of only a  
277 few photons, signal levels which would otherwise be lost beneath the readout  
278 noise of a standard CCD.

279 EM-CCDs have many uses, from 24-hour surveillance to military imaging at  
280 night. The flexibility of the camera has led to the technology being exploited  
281 in night-time surveillance [26], scientific imaging [27] and medical imaging  
282 [28]. The EM-CCD shares the same basic structure as a standard frame-  
283 transfer CCD. The main difference between the EM-CCD and a standard  
284 frame-transfer CCD is the addition of a gain register following on from the  
285 standard readout register.

### 286 5.2 *The gain process*

287 When an electron passes through a region of high-electric field it can be ac-  
288 celerated. If an electron passes through a region of high electric-field in silicon  
289 then the electron can gain sufficient kinetic energy to effectively slam into the  
290 lattice, breaking the silicon-silicon covalent bonds, the process of ‘impact ion-  
291 isation’ [21]. The generated electrons can in turn gain enough kinetic energy  
292 to break further bonds, creating extra electron-hole pairs and causing further  
293 impact ionisation.

294 Although this process can generate spurious signal through the formation of

295 electron-hole pairs from non-signal electrons, the process can be controlled  
 296 through the application of specific voltages to a specially designed gain struc-  
 297 ture in the CCD where the probability of impact ionisation increases as the  
 298 electric-field increases in magnitude. Varying the voltage applied to the multi-  
 299 plication electrode structure alters the electric-field and allows the gain process  
 300 to be controlled.

301 Due to the stochastic nature of the multiplication gain, during the gain process  
 302 each signal electron can be assumed to behave independently and may generate  
 303 a different number of avalanche electrons. The excess noise factor,  $F$ , a measure  
 304 of the ratio of the noise on the signal at the input to the gain register compared  
 305 to that at the output (for optical photons) where  $G$  is the total multiplication  
 306 gain,  $\sigma_{n_{in}}^2$  is the variance on the signal before the gain process and  $\sigma_{n_{out}}^2$  is the  
 307 variance of the output signal, is defined as [29]:

$$308 \quad F^2 = \frac{\sigma_{n_{out}}^2}{G^2 \sigma_{n_{in}}^2} \quad (2)$$

309 For a large number of transfers across the gain register (as found in the EM-  
 310 CCDs produced by e2v technologies), this formula can be solved [6] to produce:

$$311 \quad F^2 = \frac{2G - 1}{G} \quad (3)$$

312 To a first approximation,  $F$  tends to  $\sqrt{2}$  for high gain factors (tens to hun-  
 313 dreds) [29]. For optical photons the variance on the signal levels measured,  
 314 assuming Poisson statistics are valid, is equal to the mean signal level, there-  
 315 fore although gain process allows low-signal levels to be increased above the  
 316 readout noise, the noise on the signal level itself increases [29]. For very low  
 317 signal levels where high levels of gain are required, the gain process effectively  
 318 doubles the variance on the signal level. The impact of this increase in noise  
 319 will be considered further in Section 8.2. It is worth noting that this is only the  
 320 case for optical photons. If direct detection of X-rays was to be used, where  
 321 the Fano factor must come into consideration, the noise on the gain process  
 322 becomes more complicated [30].

## 323 6 EM-CCD based gamma-cameras

324 The use of off-chip signal amplification can be replaced by the use of an  
 325 Electron-Multiplying CCD (Section 5.1), such as in the early development  
 326 of the Ultra Gamma Camera (UGC) [31]. In this case, a 1 mm thick CsI(Tl)  
 327 layer was coupled to an EM-CCD through the use of a fibre-optic taper. The

328 EM-CCD used contained rectangular pixels ( $20 \times 30 \mu\text{m}$ ), resulting in differ-  
329 ent spatial resolutions in the two dimensions of  $60 \mu\text{m}$  and  $100 \mu\text{m}$  at  $122 \text{ keV}$ .  
330 Using the peak signal in each event detected, ‘energy peaks’ can be observed  
331 at  $122 \text{ keV}$  and  $28 \text{ keV}$  using two different sources, although the broadening  
332 of the spectrum to lower energies causes an overlap with the  $28 \text{ keV}$  peak such  
333 that one cannot determine the origin of photons measured at lower energies  
334 (if both sources were present).

335 Each X-ray interacting in the scintillator will do so at a different depth and  
336 will therefore generate a signal at the EM-CCD with a differing ‘spread’: the  
337 so called ‘depth of interaction’ (DOI) effect. Early attempts at producing an  
338 energy spectrum from interacting events detailed in [31] use the peak signal in  
339 an event as a measure of the energy of the X-ray interacting. Whilst this gives  
340 ‘energy peaks’, the DOI effects broaden the spectrum such that the broad  
341 peaks overlap on a large scale.

342 Developments in energy detection techniques in an attempt to remove scat-  
343 tered events produce improvements in the spectrum, but energy resolutions  
344 of  $40 \text{ keV}$  and  $42 \text{ keV}$  at  $122 \text{ keV}$  and  $28 \text{ keV}$  respectively [32] show that the  
345 technique is limited in comparison to the previously discussed detectors. A  
346 higher detector resolution combined with energy discrimination capabilities  
347 has been said to be essential for future Single Photon Emission Computed  
348 Tomography (SPECT) systems [33], but measurements of the energy resolu-  
349 tion of  $33 \text{ keV}$  at  $140 \text{ keV}$  left a requirement for further study, despite the  
350 improvements in the spatial resolution. More recently, a spatial resolution of  
351  $59.4 \mu\text{m}$  was reported using a CCD97 [34].

352 The method used to extract the energy spectrum from the raw X-ray inter-  
353 action events in the scintillator recorded in the EM-CCD has a major im-  
354 pact on the energy resolution achieved. Developments to incorporate binning  
355 of the signal in each event begin to take into account the DOI effects that  
356 are ignored in simple ‘peak signal’ techniques. However, DOI effects can be  
357 approached from two further directions. A Maximum Likelihood Estimation  
358 (MLE) technique was used in [14], incorporating a calibration stage in the de-  
359 vice development, aiming to use recorded events of known DOI to determine  
360 the DOI of events recorded when imaging. The second approach makes use of  
361 ‘scale-space’, a form of Wavelet transform, developed from algorithms used in  
362 computer vision [35], adapted to improve the resolution of gamma-cameras [3].  
363 Applications of these techniques to improve the resolution of cameras showed  
364 great promise when applied to simulated data [3] and have been further devel-  
365 oped with respect to experimental data [4] using the camera described below.  
366 The same technique has also since been detailed in [36] in which it was found  
367 to offer significant improvements over the techniques described above (as in  
368 [32]), although still limiting the energy resolution a best-case of over 40%  
369 energy resolution at  $140 \text{ keV}$  and a spatial resolution of  $59 \mu\text{m}$ .

## 370 7 Event separation

371 The results shown in Figure 3 are taken from a Monte Carlo simulation de-  
372 signed to investigate the influence of the re-absorbed fluorescence on the spa-  
373 tial resolution of the detector. A ‘block’ of scintillator, CsI(Tl) has been sim-  
374 ulated with dimensions of  $1\text{ cm} \times 1\text{ cm} \times t\text{ }\mu\text{m}$ , where  $t$  is the scintillator  
375 thickness (here shown at  $70\text{ }\mu\text{m}$ ,  $350\text{ }\mu\text{m}$  and  $700\text{ }\mu\text{m}$ ). A set flux of incident  
376 photons is entered into the system along the normal to the imaging plane  
377 using a random distribution in the  $xy$  plane. Each incident photon to the sim-  
378 ulation is generated with a randomly generated interaction distance (based  
379 on the interaction length) that will either fall within or outside of the block  
380 of scintillator. Photons that do not interact within the scintillator are lost  
381 from the system. Photons that interact within the scintillator, using standard  
382 Monte Carlo techniques, will generate a fluorescence X-ray as appropriate  
383 based on the probabilities discussed in Section 2. If a fluorescence X-ray is  
384 emitted, then this photon will travel in a randomly generated direction away  
385 from the production position and this is then tracked until interaction or exit  
386 from the scintillator structure (as with the primary photons). All locations of  
387 interactions are recorded and the distance travelled in the  $xy$ -plane (the plane  
388 of the detector pixels) is then calculated and this is shown in the distribu-  
389 tions in Figure 3. The incident photons are able to interact at any position  
390 in the scintillator as determined by probability of interaction defined by the  
391 interaction length and the scintillator dimensions. This ‘realistic’ positioning  
392 of the initial interaction positions ensures the emitted fluorescence photons  
393 will pass through the scintillator having been generated across the scintillator  
394 with no bias. If one considers the distance between the primary and secondary  
395 interaction positions from the simulated results shown in Figure 3, it is clear  
396 that negligible signal will be detected outside a millimetre in radius from the  
397 primary interaction location.

398 With a spatial resolution of the order of 0.5 millimetres and above, one is  
399 forced to consider the majority of primary and secondary events as ‘single’  
400 events. In this way, the sum of the energy deposited in the primary and sec-  
401 ondary interactions is recorded for this ‘single’ event, albeit with a bias on  
402 the positioning of the interaction position from this combination of the origi-  
403 nal interaction and the re-absorbed fluorescence X-ray, further degrading the  
404 spatial resolution.

405 Despite the apparent limits on the spatial resolution, the grouping of the  
406 energy deposited from primary and secondary interactions leads to a high  
407 spectral resolution (as high a resolution as 6% FWHM at 140 keV and 3%  
408 FWHM at 662 keV [37]). The presence of the secondary interactions has a  
409 major impact on not only the ability to achieve a higher spatial resolution,  
410 but also a major impact on the spectral resolution of the detector.

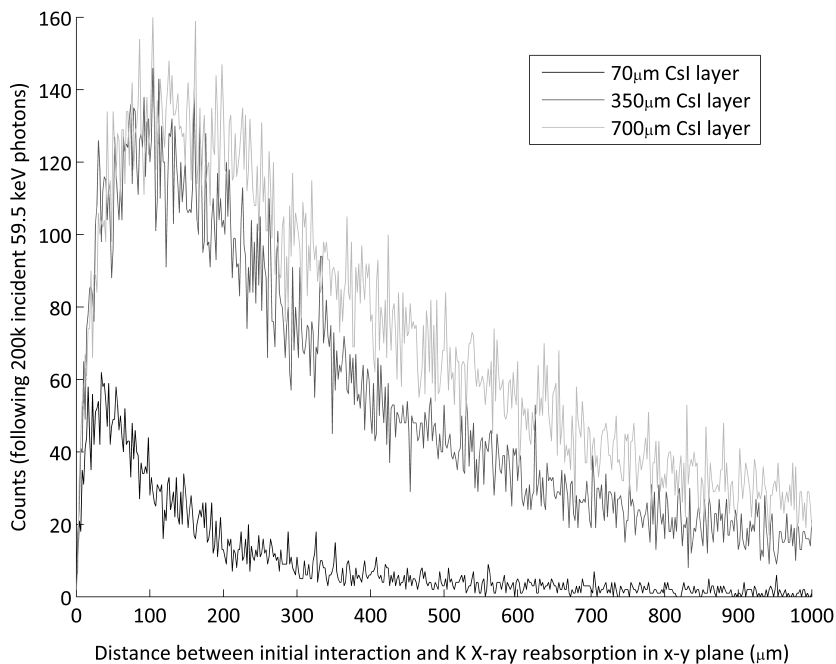


Fig. 3. The interaction distance for the fluorescence X-ray produced in CsI, simulated here for scintillator thicknesses of 70  $\mu\text{m}$ , 350  $\mu\text{m}$  and 700  $\mu\text{m}$  with a constant incident flux. The results are presented in the  $xy$  plane only, as this is the plane in which an image would be taken. As the distance approaches 1 mm, it is seen that the number of counts has rapidly decreased.

## 411 8 Scintillator-coupled EM-CCD

412 In order to demonstrate the spatial and spectral capabilities of a gamma cam-  
 413 era designed for high spatial resolution applications, a 70  $\mu\text{m}$  columnar CsI(Tl)  
 414 scintillator layer has been coupled to an e2v CCD97 [38] through a fibre-optic  
 415 plate (approximately 3 mm thick). The CCD97 has been operated here with a  
 416 pixel readout rate of 1 MHz for demonstration purposes but can be operated  
 417 at up to 15 MHz with appropriate drive electronics. The increased amplifier  
 418 noise introduced through increasing the readout rate has a negligible impact  
 419 on the image output from an EM-CCD detector as the multiplication gain can  
 420 simply be increased to reduce the effective readout noise to the sub-electron  
 421 level [25].

### 422 8.1 Photon-counting

423 The standard operation of a CCD-scintillator imaging system, such as those  
 424 used in dental imaging, involves the integration of signal over a pre-defined  
 425 period of time. During this time period, any light generated in the scintillator

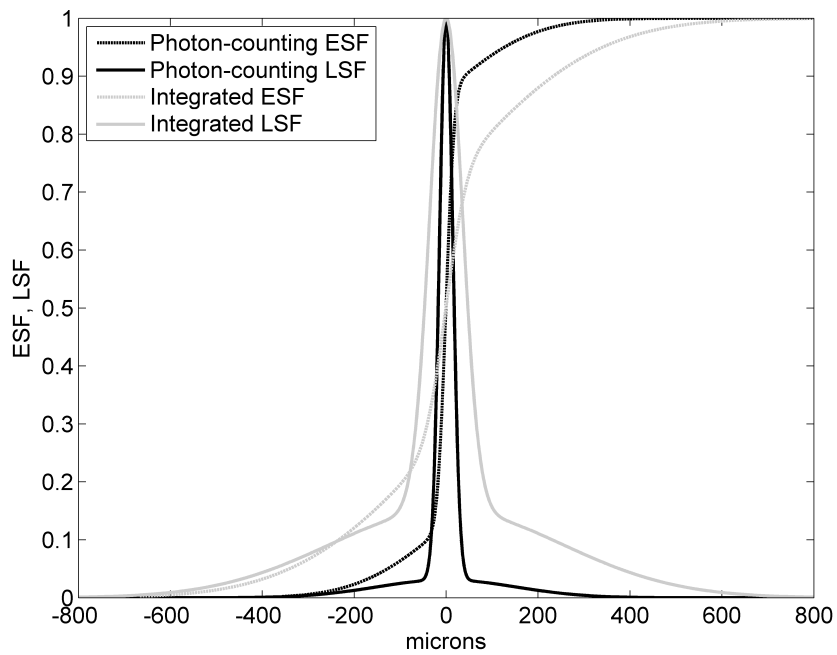
426 that is collected by the CCD will be summed to create a single contrast image.  
427 Any spread of light in the scintillator away from the initial interaction location  
428 will be summed in the image, degrading the spatial resolution by adding a  
429 secondary (wider) Gaussian profile in the Edge Spread Function (ESF), thus  
430 causing the rapid drop in MTF at low spatial frequencies, Figure 4(a).

431 An alternative method of operation involves the capture of many images over  
432 much shorter integration times such that each image contains a number of indi-  
433 vidual interactions, with each interaction separated by several pixels from the  
434 next. Through the analysis of a batch of images of this type, one can improve  
435 the imaging capabilities of the camera system dramatically. This ‘photon-  
436 counting’ technique is not straightforward and there are many factors that  
437 must be overcome, such as the impact of the depth of the primary interaction  
438 in the scintillator on the spread of the event observed by the detector [3]. Once  
439 these challenges have been considered, the batch of images can be analysed  
440 using a variety of methods on an event by event basis (Section 6).

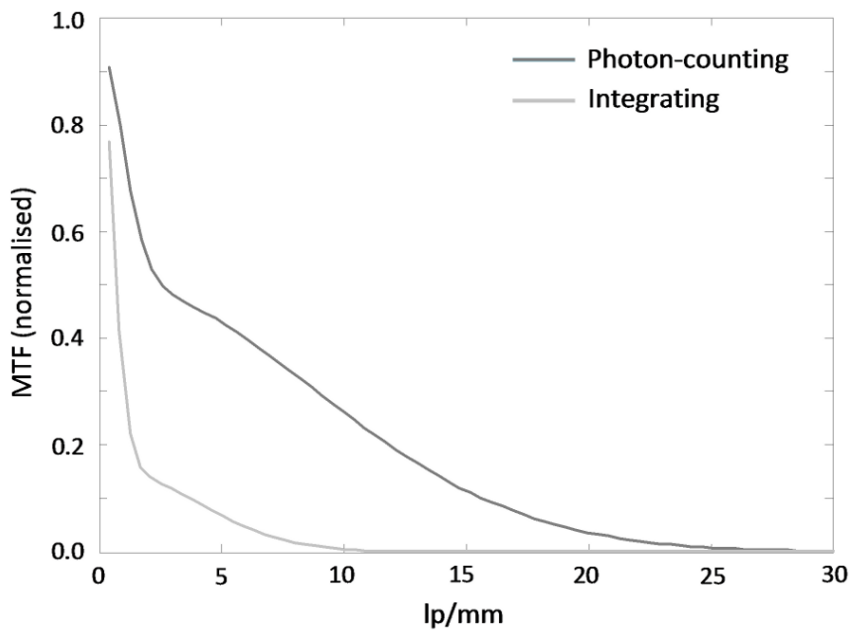
441 A simple tungsten edge was placed against the scintillating layer to act as a  
442 mask to the incident X-ray photons, in this case emitted from a solid  $^{241}\text{Am}$   
443 source (59.5 keV) with an activity of 18.4 kBq at the time of the experiment.  
444 The 0.5 mm thick tungsten edge prevents approximately 95% [39] of the inci-  
445 dent 59.5 keV photons from reaching the scintillator. The transmitted photons  
446 produce a small reduction in contrast between the covered and uncovered ar-  
447 eas of the CCD97. The active area of the  $^{241}\text{Am}$  source is in the form of a  
448 disc of diameter 5 mm. A thin layer of silver foil is present in the source  
449 holder, contributing a small amount of  $\text{K}\alpha$  X-ray fluorescence with an energy  
450 of 22 keV to the lower energy peaks in the spectrum. With the source placed  
451 at a distance of 4 cm from the tungsten edge, the geometry of the system  
452 broadens the spatial resolution that is measured, giving a spreading of the  
453 incident photons ‘under the tungsten edge’ across a width of approximately  
454  $6\pm 2$  microns (depending on the exact alignment) on the back surface of the  
455 scintillator due to the angular incidence of the X-rays. Further improvements  
456 in the measured spatial resolution would be expected if a columnar beam of  
457 incident photons was supplied to the system, but the arrangement used here  
458 allows a proof of concept study to be undertaken in which the results can be  
459 compared with that of the ‘low resolution gamma cameras’ discussed earlier.  
460 K series tungsten fluorescence is of too high an energy to be generated from  
461 the 59.5 keV incident photons (the K absorption edge for Tungsten has an  
462 energy over 59.5 keV) and the L series fluorescence (12.6 keV and below) will  
463 be removed during thresholding of the images if present.

464 Following the extraction of the individual events from the images using a tech-  
465 nique described in [4] where it is possible to adjust the event selection criteria  
466 to fit the detector environment and application, it is possible to centroid the  
467 events such that a new ‘integrated’ image can be created from the individual





(a) Line Spread Function (LSF) and Edge Spread Function (ESF).



(b) Modulation Transfer Function (MTF).

Fig. 4. Fits taken to experimental data at 60 keV in integrating and photon-counting modes. (a) The LSF is not formed from a single Gaussian profile but is instead formed from the sum of two independently characterised profiles. (b) The resulting MTF, taken as the discrete Fourier transform of the LSF, showing the ‘knee’ in the curve due to the two components of the LSF. [2]

468 centroid locations. Through the use of this process, one can remove the effect  
 469 of the spread in the light generated in the scintillator.

## 470 8.2 Spatial resolution

471 Experimental results presented in [2] detail the spatial capabilities of such a  
 472 detector, as summarised in Table 1 and Figure 4. It must be noted that the line  
 473 spread function (LSF) is not formed from the standard Gaussian-like profile.  
 474 The complication in the ESF and LSF profile introduced was proposed to be  
 475 due to the addition of a secondary Gaussian component to the LSF (such that  
 476 profile can be fitted with the sum of two Gaussian profiles, both centred at  
 477 the same position) due to re-absorption of the internal fluorescence X-rays  
 478 [2]. A narrow profile represents the standard detector LSF with a broader  
 479 component found at a lower count rate.

Imaging method	FWHM of LSF
Integration (standard)	80 $\mu\text{m}$
Photon-counting	31 $\mu\text{m}$

Table 1

Spatial resolution measurements for the scintillator-coupled EM-CCD in integrating and photon-counting modes [2].

## 480 8.3 Spectral resolution

481 With the approximately linear relationship between the light output of the  
 482 scintillator and the incident photon energy, several methods are available to  
 483 produce an energy spectrum of events. The use of the photon-counting mode  
 484 is essential for this purpose; in the integrating mode all energy information is  
 485 lost. The most simple method involves the use of the peak intensity of each  
 486 event [31]. This does not, however, make allowances for the variation in the  
 487 event profiles with depth of interaction in the scintillator, hence producing sub-  
 488 standard results. This method can be improved through the summation of the  
 489 central pixel of the events with surrounding pixels, now including the edges of  
 490 the Gaussian profiles [2]. Unfortunately, for every extra pixel included in this  
 491 summation, additional noise is also included. Using more complex methods,  
 492 such as the use of Scale-Selection as discussed in [3,5,36], one is able to produce  
 493 more detailed information about each event, such as the inference of the depth  
 494 of interaction in the scintillator from the spread of the photons in the event  
 495 profile.

496 With the requirements on detectors to enable high-resolution imaging, the  
 497 detector noise is a limiting factor unless an EM-CCD is used to reduce the ef-

498 fective readout noise to the sub-electron level. In reducing the effective readout  
 499 noise, one must use a gain process to increase the number of signal electrons.  
 500 This gain process introduces an approximate increase in the noise level on the  
 501 signal of  $\sqrt{2}$  (as discussed in Section 5.2). Taking an  $^{241}\text{Am}$  event in  $70\ \mu\text{m}$  of  
 502 CsI(Tl), as implemented in [2], a peak signal (in the central pixel of an event  
 503 hitting the centre of a pixel) of approximately 40 photons was measured when  
 504 considering the 30 keV components that dominate the spectrum. If a more ef-  
 505 ficient coupling mechanism is used between the scintillator and detector then  
 506 it is possible to increase the number of photons detected, whilst if a less ef-  
 507 ficient coupling mechanism is used then fewer photons may be recorded. If a  
 508 fibre-optic taper is used, one must include the associated losses involved. The  
 509 directly neighbouring pixels were found to have 5-25 photons each (dependent  
 510 on photon hit position in the pixel) in the previous study [2]. Using simulated  
 511 Gaussian profiles one is able to determine a ‘best-case’ energy resolution from  
 512 an approximation to the light spread, multiplication noise components and  
 513 intrinsic scintillator resolution. The results presented in Figure 5 are based on  
 514 the experimental results with respect to the form of the event profiles achieved  
 515 with the CsI(Tl) detector system detailed in this paper and literature values  
 516 are used for the comparisons to NaI(Tl) and LaBr<sub>3</sub> and for the incorporation  
 517 of the fibre-optic tapers [8,40]. These predicted results compare well with the  
 518 experimental system detailed in Section 8, taking measurements from the ex-  
 519 perimental spectra shown in Figure 7, and demonstrate that there are indeed  
 520 limitations on the energy resolution achievable with such systems formed from  
 521 scintillator-coupled EM-CCDs. In comparison to the specific experimental de-  
 522 tector system detailed in this study and the spectra recorded for Am<sup>241</sup> and  
 523 Co<sup>57</sup>, it can be seen in Figure 5 that the performance is verging on the intrinsic  
 524 performance limits achievable with such coupling.

## 525 9 Simulating a scintillator-based gamma-camera

526 In order to facilitate a better understanding of the camera system, several  
 527 new simulations have been produced, allowing the demonstration and expla-  
 528 nation of the effects noted in previous experimental studies and investigation  
 529 of their impact. The energy deposition and localisation in the scintillator has  
 530 been simulated, making use of the interaction lengths of each photon energy  
 531 in the scintillator (CsI in this case). Using a three dimensional scintillation  
 532 body, random directional generation for each X-ray photon following interac-  
 533 tion in the scintillator allows the position of the event profile in the plane of  
 534 the EM-CCD to be modelled. The interaction chain for the simulation is based  
 535 on Figure 6, detailing the emission and re-absorption (or loss) of fluorescence  
 536 photons. From the experimental results of [2] it was suggested that the ‘two  
 537 Gaussian’ profile of the LSF was caused by the re-absorbed fluorescence com-

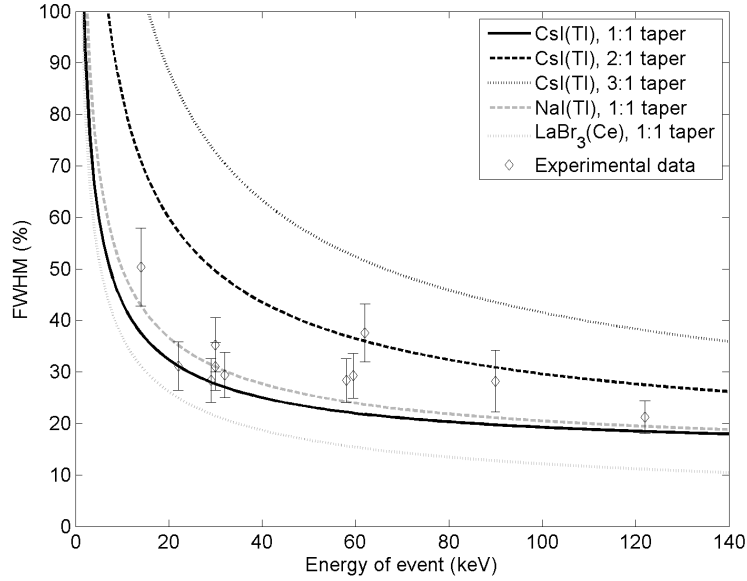


Fig. 5. Expected best-case energy resolution for the experimental camera system (CsI:Tl with a 1:1 fibre-optic taper) over a range of energies. Literature values for different scintillators [8] have been incorporated to predict the performance of similar systems following a change in scintillator or fibre-optic taper. The experimental results taken from Figure 7 for  $\text{Am}^{241}$  and  $\text{Co}^{57}$  are shown for comparison with the theoretical calculations and demonstrate that the detector detailed in this study is verging on the intrinsic limits for the coupling system used.

538 ponent, resulting in the curvature at the edges of the ESF (Figure 4(a)). These  
 539 simulations aim to demonstrate the effect of the imaging of the fluorescence  
 540 X-rays through a test-case simulation of the “perfect detector”. The “perfect  
 541 detector” is assumed to have an MTF of one across all spatial frequencies and  
 542 a scintillator in which the visible photons generated in the scintillator do not  
 543 spread out as they pass towards the EMCCD. Therefore any degradation in  
 544 resolution (or degradation of the ESF from a simple step function) is caused  
 545 by the detection of the X-ray fluorescence. Also of interest here is the impact  
 546 of the interaction chain (as detailed in Figure 6) on the spectral performance.

### 547 9.1 Spectral performance

548 Two spectra, measured using the experimental set-up detailed in Section 8.1  
 549 using a CCD97 and CsI(Tl) scintillator, for  $\text{Am}^{241}$  (18.4 kBq) and  $\text{Co}^{57}$  (70 kBq)  
 550 are shown in Figure 7 (data points, [4]). The CCD97 was operated in inverted  
 551 mode at  $-20 \pm 5^\circ\text{C}$  (to suppress dark current) at a readout rate of 1 MHz (0.3  
 552 seconds per frame), with approximately  $10^5$  frames analysed for  $\text{Am}^{241}$  and  
 553  $1.7 \times 10^4$  frames analysed for  $\text{Co}^{57}$  (a large number of frames was required due  
 554 to the low activity of the source). A higher frame rate and a source with a

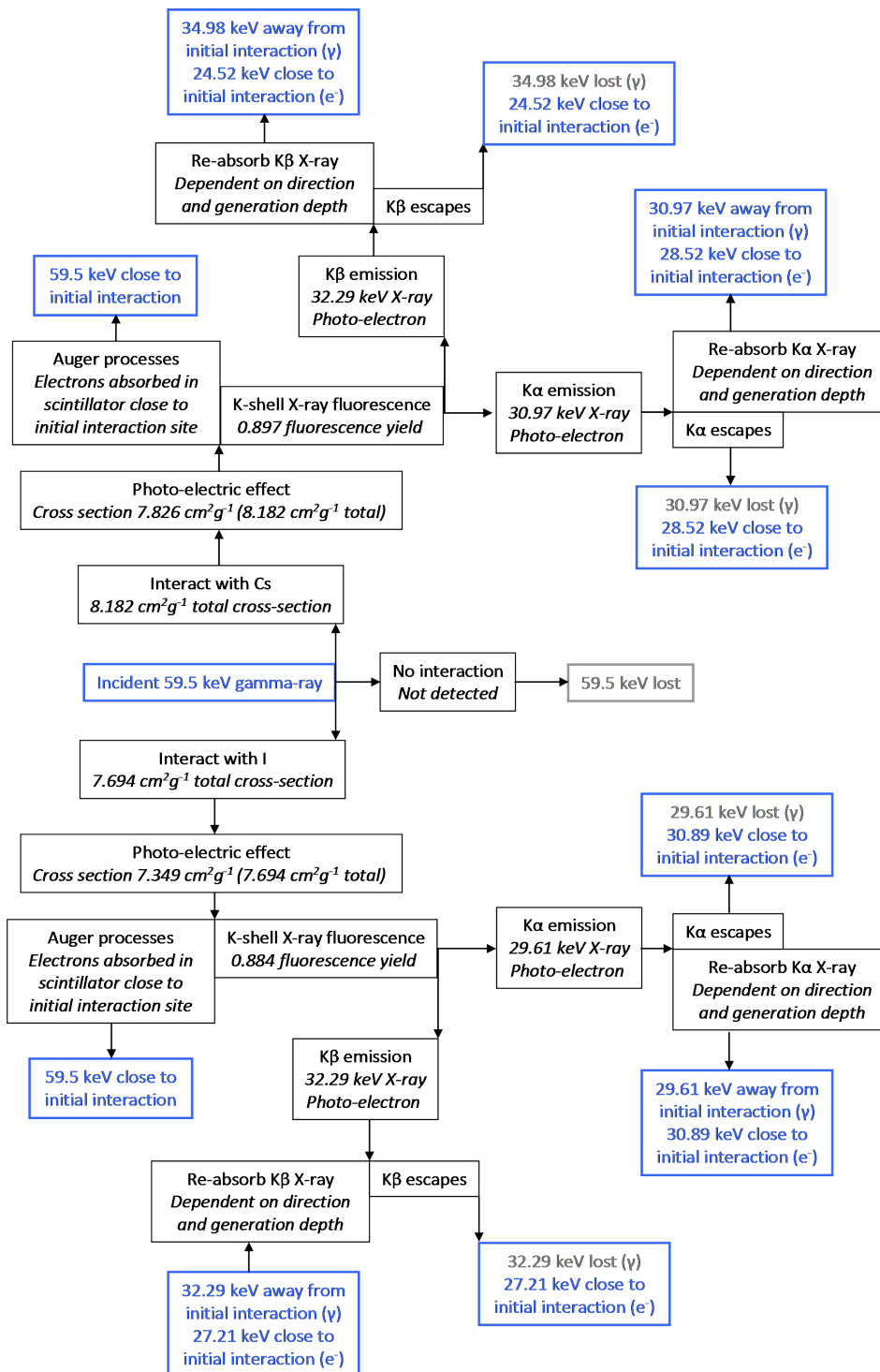


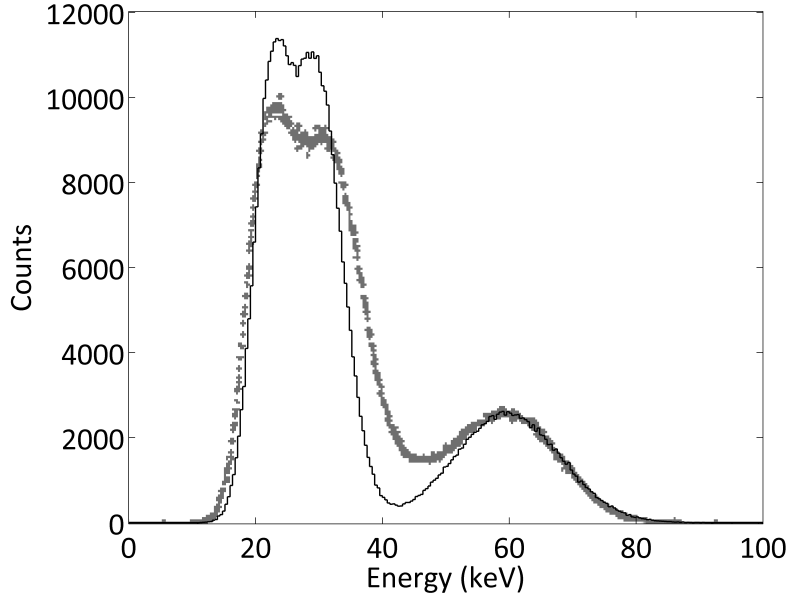
Fig. 6. Flowchart of the interactions incorporated into the simulation process for irradiation of CsI by 59.5 keV gamma-rays.

555 higher activity could be easily implemented into the system with appropriate  
556 electronics and source availability; the increased readout noise from the in-  
557 creased readout speed can be counteracted by an increase in the gain applied  
558 with the EM-CCD to remain at an effective readout noise of 1 electron rms.  
559 The total number of interactions recorded per frame is the only limit on the  
560 activity at any readout speed, such that events must not overlap (no pileup)  
561 for the centroiding of individual events to be possible.

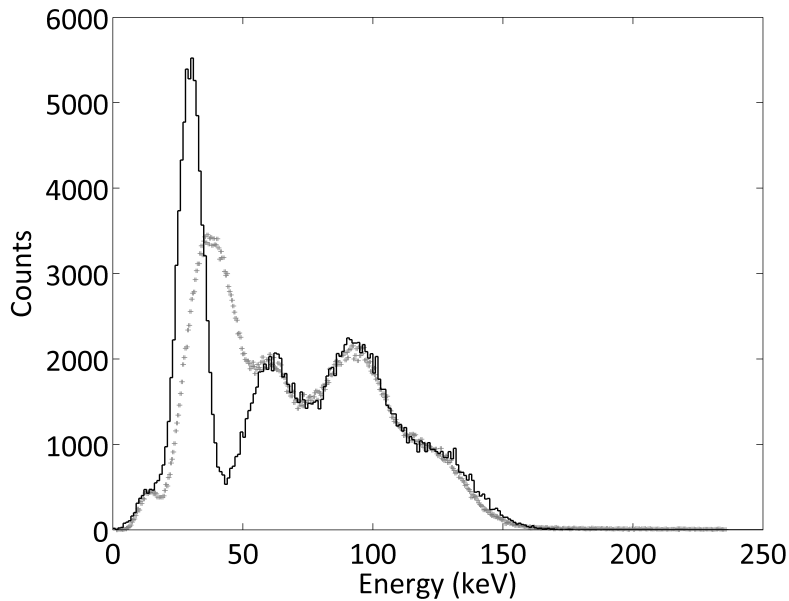
562 The spectrum achieved using Am<sup>241</sup> shows how the peak at approximately  
563 30 keV dominates over the full-energy peak at 59.5 keV. The peak at approx-  
564 imately 30 keV is formed from many components, namely the re-absorbed  
565 fluorescence ( $K\alpha$  and  $K\beta$  from both Cs and I), the related escape peaks and  
566 fluorescence from the silver foil in the <sup>241</sup>Am source. With the limits on the  
567 spectral resolution incurred from the intrinsic scintillator resolution and the  
568 multiplication gain noise, one cannot separate out the re-absorbed fluorescence  
569 events (located away from the primary photon interaction position) from the  
570 escape events (at the primary photon interaction position). It is only possi-  
571 ble, therefore, to exclude ‘all events’ around 30 keV in order to remove the  
572 re-absorbed fluorescence and therefore to reduce the overall number of counts  
573 dramatically by removing the escape events. In this respect, it is therefore  
574 essential to determine the requirements of the imaging system and consider a  
575 spatial resolution versus count rate trade-off. In the case of the Am<sup>241</sup> spec-  
576 trum, there is an element of separation between the peaks at 30 keV and  
577 the full-energy peak and therefore one can improve the resolution in the case  
578 where this is the priority over the number of counts measured (see Section 11).

579 The simulated results shown in Figure 7 take the simulation of events dis-  
580 cussed in Section 9 and incorporate the energy resolutions shown in Figure 5,  
581 measured from the experimental results; each event generated in the simula-  
582 tion has a “recorded energy” randomly generated across a Gaussian profile.  
583 The simulations include full-energy events,  $K\alpha$  and  $K\beta$  fluorescence from the  
584 caesium and iodine in the scintillator, the related escape events and  $K\alpha$  fluo-  
585 rescence from silver (in the <sup>241</sup>Am case) and tungsten (in the <sup>57</sup>Co case), with  
586 the quantity of external fluorescence (silver or tungsten as appropriate) set as  
587 a free parameter to be fitted with the experimental data due to the complex  
588 geometries and uncertainties involved in quantising the number of fluorescent  
589 X-rays generated and subsequently detected.

590 Taking the case of the <sup>241</sup>Am spectrum, Figure 7(a), the appropriate structure  
591 can be clearly seen in the simulated results as normalised to the intensity of  
592 the 60 keV peak. However, the simulated peak at approximately 30 keV is seen  
593 to be higher than that in the experimental results, with a dip in the simulated  
594 results at approximately 30-50 keV. This discrepancy between the simulated  
595 and experimental results is thought to be due to the methods used to calculate  
596 the energy of each event in the experimental case. The overestimation in the



(a) Experimental spectra for  $\text{Am}^{241}$  (data points) and the simulated spectrum (solid line).



(b) Experimental spectra for  $\text{Co}^{57}$  (data points) and the simulated spectrum (solid line).

Fig. 7. (a) The spectrum achieved experimentally from the  $\text{Am}^{241}$  source (data points, [4]) shows the components at the energies specified in the flowchart from Figure 6. A cut-off at approximately 40-50 keV allows the removal of some of the reabsorbed fluorescence, but this removes the bulk of the escape events also and therefore dramatically reduces the number of counts. (b) The experimental spectrum obtained using  $\text{Co}^{57}$  (data points, [4]) can be explained following a similar analysis as shown in Figure 6 but for  $\text{Co}^{57}$ . The peak at approximately 60 keV is thought to be the detection of  $\text{K}\alpha$  fluorescence from the tungsten edge.

597 peak at approximately 30 keV is approximately equal to underestimation of  
598 the spectrum around 40 keV. Although the simulation accounts for directly  
599 coincident events, interactions in close proximity that are not counted as single  
600 events lead to an increased energy being attributed to some events, Figure 8.  
601 It is thought that the dip in the simulated spectrum can be accounted for in  
602 this way.

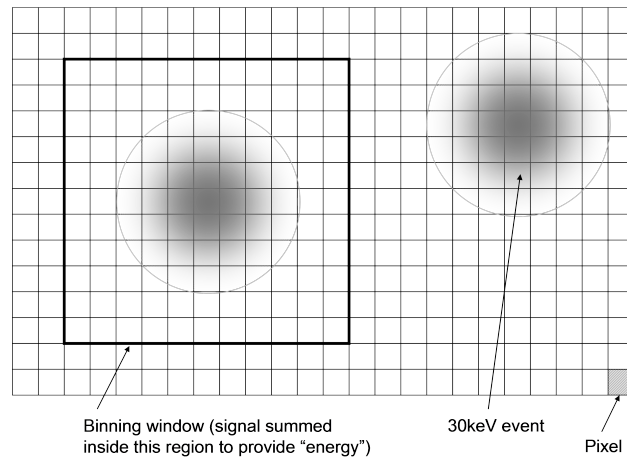
603 In order to demonstrate the further complications that occur when using a  
604 higher energy gamma source, the 122 keV photons from a  $\text{Co}^{57}$  were imaged  
605 and a similar spectrum produced, Figure 7(b). A similar analysis to that de-  
606 tailed in the flowchart in Figure 6 can be used to determine the multiple  
607 energies that will be detected from the 122 keV source, including fluorescence  
608 from the tungsten edge at approximately 60 keV and the related escape peaks  
609 (noting the spectrum achieved from the incident 59.5 keV photons from the  
610 previous testing with the  $\text{Am}^{241}$  source). In decreasing energy, the full-energy  
611 peak can be seen at 122 keV, but this is not fully resolvable from the escape  
612 peak at approximately 90 keV. The fluorescence of the tungsten edge can  
613 be seen at approximately 60 keV. The large peak at approximately 30 keV is  
614 formed from several components, namely the reabsorbed fluorescence from the  
615 122 keV incident X-rays and the reabsorbed fluorescence (and corresponding  
616 escape peaks) from the tungsten fluorescence. The low energy peak at 14 keV  
617 is due to emission from the  $\text{Co}^{57}$  source at this energy (although much of  
618 this has been removed through thresholding). Taking these energies, it is pos-  
619 sible to separate the spectrum into the related components, Figure 7(b). In  
620 this case, the spatial coincidence of fluorescence, escape and primary events  
621 is greatly complicated by the inclusion of the fluorescence from the tungsten  
622 edge and the corresponding K-shell fluorescence of the scintillator.

623 The simulation has again been run for the case of the  $^{57}\text{Co}$  and the results  
624 shown in Figure 7(b). As detailed for the  $^{241}\text{Am}$  case, the intensity of the  
625 lower energy peak is overestimated in the simulation, followed by a similar dip  
626 around 40 keV. This is thought to be for the same reasons as detailed in the  
627  $^{241}\text{Am}$  case, as outlined in Figure 8.

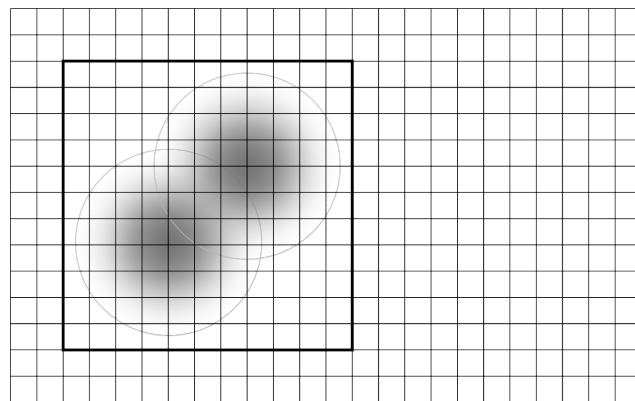
628 In the case of higher energy sources, therefore, the improvement of the spa-  
629 tial resolution through the removal of fluorescence events must be considered  
630 as somewhat more complex. Through the removal of low energy events (for  
631 example, below 50 keV), one can remove the re-absorbed fluorescence and  
632 leave a higher number of full-energy and escape events than in the  $\text{Am}^{241}$   
633 case detailed above. However, the detection of many escape events (due to the  
634 potential increased overlap between primary energy peak and escape peak)  
635 can leave a minor degradation of the spatial resolution from the range of the  
636 electrons emitted of a few micrometers for each interaction.

637 The energy resolution measured for the main peak at 60 keV from the  $\text{Am}^{241}$

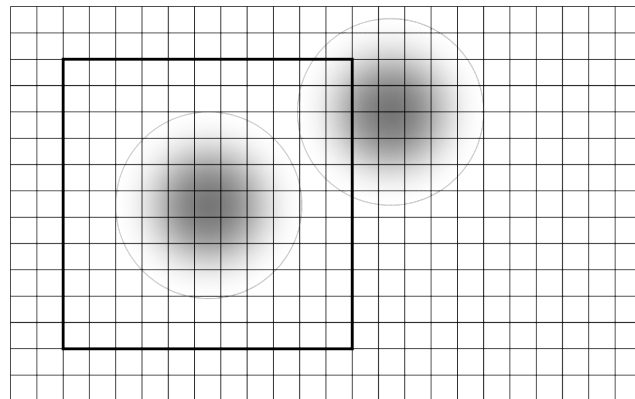




(a) Well separated events.



(b) Coincident events.



(c) Semi-coincident events.

Fig. 8. The “energy” of each event is assumed to be proportional to the summed signal over a fixed area window surrounding the peak in intensity of each event. (a) Two events have occurred across the pixilated structure of the CCD such that no signal from the second event is summed with the first. The “energy” recorded is that of the first event only. (b) Two events occur in very close proximity, such that the spread of signal from each event creates one “single” event that is recorded with the summed energy (60 keV here). (c) Two events occur a short distance apart such that a fraction of the signal from the second event is included in the “energy” recorded for the first event. The amount of “extra energy” included with the first event will vary with the distance between the events and therefore some of the low energy events will be moved to higher energies in the spectrum across a continuum from 30 keV up to 60 keV, from (a) to (b).

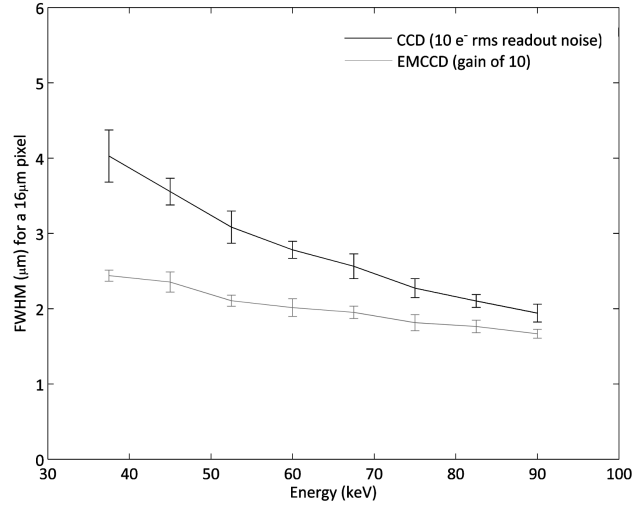
638 source in the experimental results shown is 33% (20 keV at 60 keV), converging  
639 on the limits imposed by the multiplication gain process and intrinsic energy  
640 resolution of the scintillator as demonstrated in Figure 5. This result, whilst  
641 not reaching the energy resolutions found in the literature for PMT-based  
642 gamma cameras (Section 3), the results are consistent with those reported for  
643 EM-CCD based camera systems (Section 6). The energy resolution could be  
644 improved through the more efficient coupling of the scintillator to the EM-  
645 CCD or through the use of a scintillator with a higher light output.

## 646 9.2 Positional accuracy

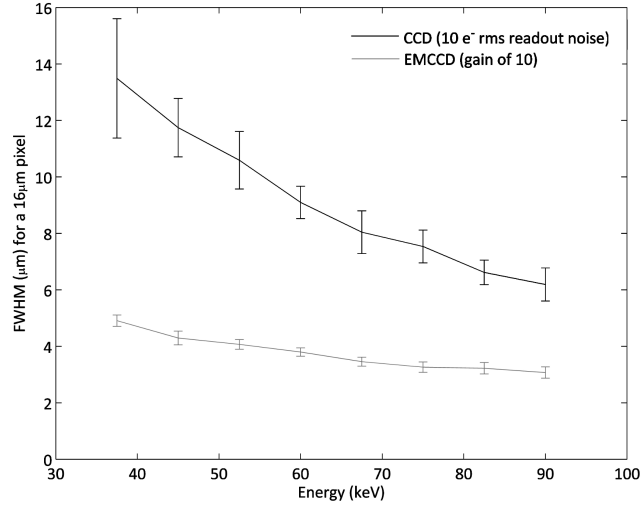
647 A second simulation has been used to look at the errors involved in the cen-  
648 troiding process when using a ‘high spatial-resolution’ gamma-camera. Cen-  
649 troiding must be used to provide sub-pixel locations for the event profiles. The  
650 sub-pixel locations can be used to create an image that no longer includes the  
651 spread of light in the scintillator (as would be found in an integrated image).  
652 It is this removal of the light spread that provides the dramatic improvements  
653 in spatial resolution detailed in Section 8.2. The noise on the signal does, how-  
654 ever, affect the centroiding process. The noise components of most importance  
655 here are the noise on the signal input to the EM-CCD, the noise on the gain  
656 process and the readout noise of the device.

657 The simulation produced for this study creates a Gaussian profile with param-  
658 eters based on the experimental data of [2]. The central point of the Gaussian  
659 profile (FWHM of 38  $\mu\text{m}$  and peak signal of 80 electrons at 60 keV, scaling  
660 linearly with energy) is positioned in the two extremes of the pixel location: in  
661 the centre and in the corner of the pixels. Edge effects are apparent in the cen-  
662 troiding process of this noiseless signal due to the use of the ‘centre of mass’  
663 approach, as one would expect, where the calculated centroid positions are  
664 biased towards the centre of the pixel. These effects can be corrected for using  
665 the  $\eta$ -algorithm [41]. One is then able to simulate the noise on the signal and  
666 add readout noise (in this case 10 electrons rms) to simulate the noise sources  
667 for an ‘equivalent non-EM CCD’ running at approximately 1-2 MHz (effec-  
668 tively the CCD97 with multiplication gain of one to allow direct comparison  
669 with the same pixel sizes). A second option is to apply gain and subsequently  
670 add the noise component from the gain process and the readout noise to sim-  
671 ulate the noise sources for an EM-CCD. The results from these tests with  
672 varying energy are shown in Figure 9, demonstrating the ‘best case’ centroid-  
673 ing performance if no other degrading factors relating to the scintillator are  
674 considered.

675 The centroid error, as shown in Figure 9, refers to the difference between  
676 the input Gaussian central location and that calculated from the centroid



(a) Centre of the pixel.



(b) Corner of the pixel.

Fig. 9. A comparison of the expected optimal centroiding accuracy using a simple  $3 \times 3$  “centre of mass” for a standard non-EM CCD as discussed previously (10 electrons rms readout noise) and an EM-CCD (with a gain of 10) from simulations of a representative Gaussian profile (FWHM of  $38 \mu\text{m}$  and peak signal of 80 electrons at 60 keV, scaling linearly with energy) placed in the centre (a) and corner (b) of a pixel. The excess noise from the gain process, when coupled with the reduction in the effective readout noise, has minimal impact and the ‘best case’ resolution improves beyond that of the standard CCD. The effects are emphasised for the corner of the pixel where the signal does not ‘peak’ in one pixel, but instead is shared over four pixels in a  $2 \times 2$  grid, with subsequent reductions in signal for the the neighbouring pixels, as defined by a Gaussian profile placed in the corner of the pixel.

677 algorithm (“centre of mass” on a  $3 \times 3$  pixel area around the pixel of peak  
678 signal) following the inclusion of the specified noise sources. Centroiding errors  
679 are provided across a range of energies relevant to this study where a 60 keV  
680 event is said to peak at approximately 80 photons for events in which the  
681 signal is centred around the centre of a pixel.

682 It is clear from Figure 9 that the EM-CCD offers improved performance over  
683 the equivalent CCD in all cases, shown here for a Gaussian with FWHM of  
684  $38 \mu\text{m}$  on a pixel size of  $16 \mu\text{m}$  for both the CCD and EM-CCD. The effects  
685 are more pronounced at lower energies as the signal-to-noise ratio is reduced in  
686 comparison to the higher energy cases. When the event signal is centred over  
687 the corner of a pixel, the peak signal, to a first approximation, may be consid-  
688 ered as almost one quarter of that in the pixel-centre case, hence producing  
689 a large reduction in the signal-to-noise ratio and therefore offering very poor  
690 spatial centroiding performance when using a standard CCD. The EM-CCD,  
691 however, performs consistently well over all energies and event locations in the  
692 pixel.

693 The simulated optimal centroiding accuracy data discussed above show that  
694 the noise on the gain process has little effect on the accuracy of the cen-  
695 troiding process, despite the added problems caused to the spectral resolution  
696 discussed in Section 8.3. If operating at the high-readout speeds required for  
697 many photon-counting applications, the readout noise of the standard CCD  
698 could be expected to be higher than the 10 electrons rms used in the simu-  
699 lations here and hence the low-noise performance of the EM-CCD becomes  
700 essential to maintain the centroiding accuracy.

## 701 **10 The impact of internal X-ray fluorescence on spatial resolution**

702 Previous experimental studies have detailed the observation of reabsorbed  
703 fluorescence events detected outside the area of imaging area [2,4,13,14]. Our  
704 simulations are consistent with hypothesis that the two Gaussians seen in the  
705 LSF, as demonstrated in Figure 4(a), result from the initial interaction events  
706 (sharper profile) and the re-absorbed fluorescence events (broader profile). The  
707 impact of the broader profile is dramatic and can be seen in the MTF curves  
708 shown in Figure 4(b) as the sharp drop in MTF at low spatial frequencies. If  
709 one was to use lower energy X-rays (with energies below the ionisation energy  
710 of the components of the scintillator) one would expect the MTF to be greatly  
711 improved, following the form of the MTF shown here at higher frequencies,  
712 but now across all frequencies.

713 *10.1 Simulating the impact of re-absorbed fluorescence on the edge spread*  
714 *function*

715 In order to separate out the impact of re-absorbed fluorescence on the spa-  
716 tial resolution of a gamma camera, all aspects of the detector itself must be  
717 removed. To this end, a simulation of a camera system with a perfect Edge  
718 Spread Function (ESF), a step-function from zero to one, was produced to  
719 match the detector used in the previously mentioned experimental programme  
720 [2]. The detector is formed from a 1 cm square CsI scintillator of thickness  
721 70  $\mu\text{m}$ . For the purposes of this simulation, all ‘detector’ aspects of the resolu-  
722 tion are to be removed, hence the interactions of photons in the scintillator are  
723 assumed to be point-like and depth of interaction effects and light spread are  
724 not included in the resulting ESF. In this way, one can separate out the purely  
725 fluorescence-induced effects. It is therefore possible to simulate the equivalent  
726 set-up to that used experimentally to determine the ESF and LSF, but here  
727 with the ‘detector’ components removed.

728 The experimental set-up has been simulated through the provision of incident  
729 photons of 60 keV to the simulation across a set area only (to simulate an  
730 effective tungsten edge). The interactions in the scintillator are tracked and  
731 the location of photon interactions in the scintillator are recorded. The re-  
732 sults produced show a clear curvature of the ESF. For the ‘perfect detector’  
733 as simulated here, one would expect a sharp step-function, however, the ESF  
734 is anything but sharply defined. The curvature is consistent with that seen  
735 experimentally and shows clearly the influence that the re-absorbed internal  
736 fluorescence has on the edge of an object being imaged, Figure 10. The recog-  
737 nisable curvature to the ESF is seen in the simulated results in which only the  
738 re-absorbed fluorescence is included; no other aspects that might degrade the  
739 detector resolution have been included. This curvature to the ‘perfect’ detector  
740 response is responsible for the secondary, broader Gaussian component of the  
741 LSF seen in the experimental results of Figure 4(a) and can be seen to stretch  
742 across several hundred micrometers as implied in Figure 3 in which the distri-  
743 bution of re-absorbed fluorescence in the  $xy$  plane is displayed. This therefore  
744 demonstrates that the secondary Gaussian in the LSF can be caused by the  
745 re-absorption of the fluorescence X-rays. In the experimental data, the ‘cur-  
746 vature’ displayed here is convoluted with the detector response (the central,  
747 more narrow, Gaussian shown in the experimental LSF, Figure 4(a)).

748 *10.2 Re-absorption distance and the energy resolution*

749 Referring back to Figure 3, one can see that for this example of using a 70  $\mu\text{m}$   
750 thick CsI(Tl) layer with an incident photon energy of 60 keV, the initial event

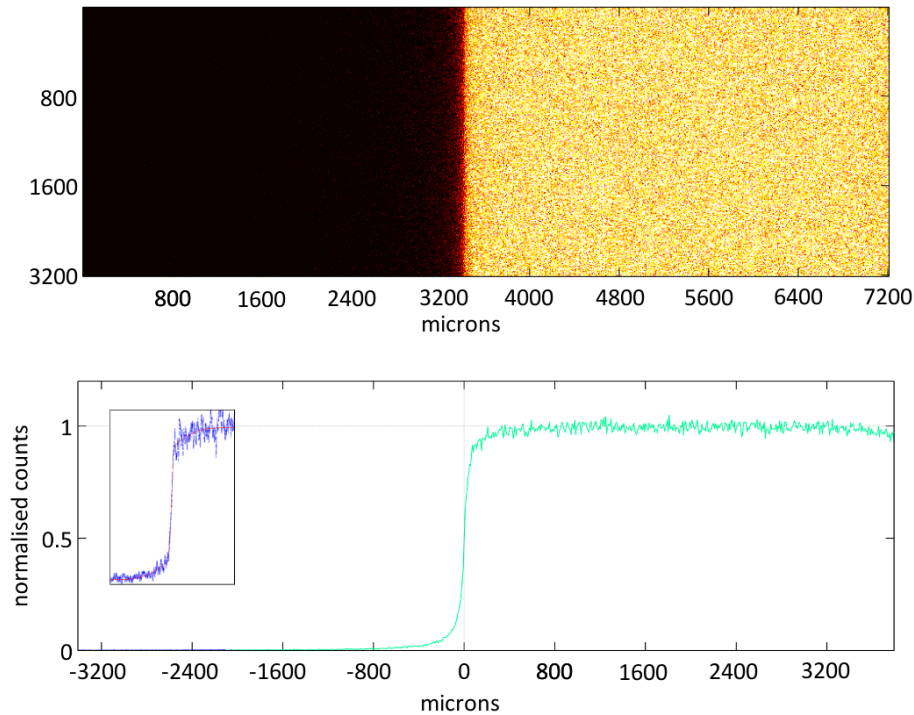


Fig. 10. Top: A simulated image of an edge for a detector system with a perfect (step-function) ESF if internal fluorescence were to be ignored. Recorded events are not limited to the right hand half of the image upon which the photons were incident to the system, showing the influence of the re-absorbed internal X-ray fluorescence (in this case for 60 keV incident photons in a 70  $\mu\text{m}$  thick CsI:Tl layer). Bottom: Without re-absorbed fluorescence one would expect a perfect step-function, with the roll-over of the signal demonstrating the presence of signal from the re-absorbed fluorescence, as displayed in the inset ESF from experimental data.

751 and the re-absorbed fluorescence X-ray will be included in the same ‘event’ if  
 752 the detector spatial resolution is of the order of a few hundred micrometres  
 753 or more. Not only is this the case, but if a much larger pixel size is used with  
 754 individual scintillator modules, one can also capture additional visible photons  
 755 from reflections occurring at the edges of the scintillation objects and it then  
 756 becomes possible to achieve energy resolutions of the order of the limits of  
 757 the scintillation process itself. With this greatly improved energy resolution,  
 758 however, comes a significant reduction in the spatial capabilities of the device  
 759 as the effective binning of the signal increases the size of each imaging ‘pixel’.

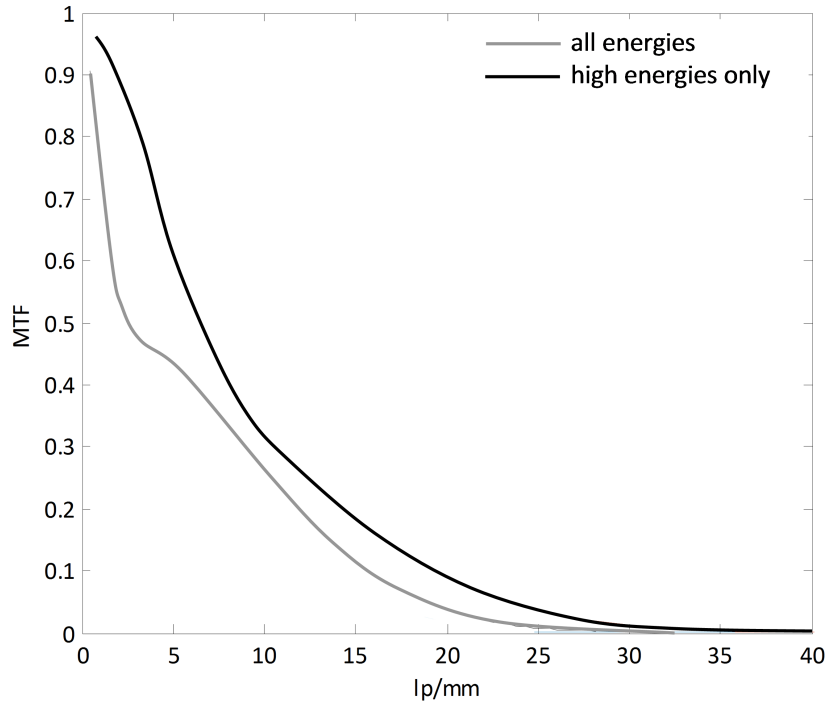


Fig. 11. Results from the same experimental campaign as detailed in Section 8. An energy threshold of 45 keV was used to remove many ‘low energy’ events and hence remove a portion of the fluorescent and escape events. The improved resolution is shown by the improved MTF across all spatial frequencies, but particularly at high spatial frequencies (a factor of 2 improvement at 20 lp/mm).

## 760 11 Reducing the impact of the internal X-ray fluorescence

761 It has been detailed in [2] that through the use of energy discrimination (using  
 762 the calculated energy of a profile through methods as described in Section 8.3)  
 763 one can remove the many of the re-absorbed fluorescence events. This process  
 764 does, however, come at a cost to the effective detection efficiency, as a large  
 765 number of primary interaction events will also be removed, leaving only ap-  
 766 proximately 10% of events for which no X-ray fluorescence occurs when imag-  
 767 ing at 60 keV. At 60 keV, for a  $^{241}\text{Am}$  source, the spatial resolution (FWHM  
 768 of the LSF) can be improved from 31  $\mu\text{m}$  to 25  $\mu\text{m}$  [2], although this improve-  
 769 ment in FWHM is mostly due to the removal of the escape electrons which  
 770 are responsible for ‘events’ recorded a few micrometers away from the initial  
 771 interaction positions. The main improvement from the energy discrimination  
 772 process is instead that of the reduction in the intensity of the broader Gaus-  
 773 sian component of the LSF, that due to the fluorescence, and hence a much  
 774 improved MTF and greatly improved imaging performance, Figure 11.

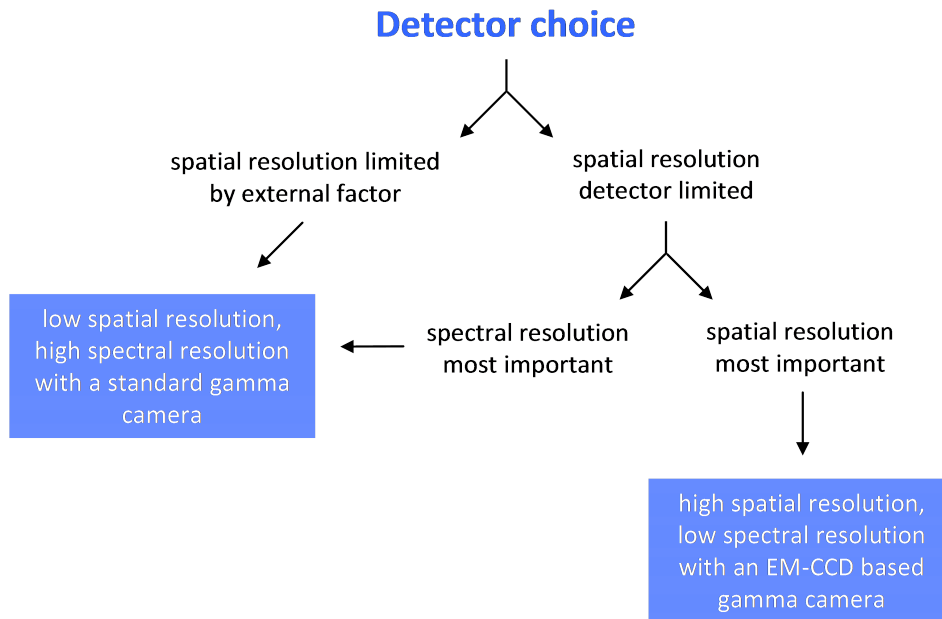


Fig. 12. Simplified summary of the most appropriate gamma camera detector choice.

## 775 12 Related detector developments

776 Over recent years, the development of hybrid pixel detectors has brought the  
 777 possibility of high spatial resolution detectors which are capable of also pro-  
 778 viding a high energy resolution. The bonding of CdTe and CdZnTe detectors  
 779 to CMOS readout chips has enabled a combined performance to be achieved,  
 780 albeit on the small area scale as one loses the option to apply optics to expand  
 781 the imaging area (such as a lens system or through fibre-optic tapering). Re-  
 782 sults reported so far include an intrinsic spatial resolution of  $75\ \mu\text{m}$  at 122 keV  
 783 in studies detailed in [20] using a CdTe pixel detector ( $14\times 14\times 1\ \text{mm}^2$ ) with  
 784  $256\times 256$  square pixels and a  $55\ \mu\text{m}$  pitch. This pixel detector is coupled to  
 785 a CMOS single photon counting integrated circuit from the Medipix2 series.  
 786 In similar early developments using a CdZnTe sensor, a FWHM (at room  
 787 temperature) at 122 keV of 2.5% has been reported [42], although no spatial  
 788 results are presented.

## 789 13 Conclusions

790 The choice of detector for X-ray imaging, as with all applications, must be care-  
 791 fully considered, as the experimental and simulated data presented here have  
 792 shown. The most appropriate choice of detector can be briefly summarised as  
 793 shown in Figure 12.



794 If the spatial resolution of a system is limited by an external factor such as the  
795 collimators used in medical imaging, then the scintillator-coupled EM-CCD is  
796 the optimal detector choice. The dramatic improvement in spatial resolution  
797 over more traditional X-ray imaging systems has negligible impact on the  
798 images taken due to the limits on the resolution set by the collimator. A lower  
799 spatial resolution system, one with a better energy resolution, should be the  
800 imaging system of choice. The spectral performance of gamma-cameras based  
801 on the PMT (Section 3) cannot be reached by current EM-CCD based systems  
802 in which the limit with CsI(Tl) has been shown to be approximately 20-30%  
803 using americium-241 with a 1:1 fibre-optic plate. Using scintillators with a  
804 higher light output would improve the spectral resolution but the increase in  
805 noise from the multiplication gain process cannot yet be overcome.

806 If one is not limited spatially by external sources, then the scintillator-coupled  
807 EM-CCD should be seriously considered. Imaging for synchrotron-based appli-  
808 cations where high resolution, high sensitivity and a high signal-to-noise ratio  
809 are required may benefit greatly from the improved spatial resolution when  
810 low fluxes are required to be measured to a high positional accuracy, although  
811 care would be required in appropriately shielding the detector from direct de-  
812 tection to prevent damage to the EM-CCD and the electronics. For example,  
813 in macromolecular crystallography, the high spatial resolution will bring the  
814 ability to better resolve closely lying distributions of peaks whilst improv-  
815 ing the signal-to-noise ratio for low intensity peaks. In systems in which the  
816 integration imaging mode is predominantly used, the improvements through  
817 photon-counting with such a detector allow the basic use of energy discrimina-  
818 tion that would not otherwise be possible. However, the energy resolution of a  
819 high-resolution gamma-camera such as this is limited by the processes through  
820 which the high spatial resolution is achieved. By using only a small proportion  
821 of the visible photons emitted by the scintillator for each event (to keep the  
822 spatial information in the form of the Gaussian-like event profile), the noise on  
823 the detected signal is comparatively high and is increased further still through  
824 the gain process of the EM-CCD (required to keep the effective readout noise  
825 low at the high frame-rates required for photon-counting imaging).

826 In systems in which the energy of the incident X-rays is lower than the K  
827 binding energy of the scintillator elements (less than approximately 30 keV for  
828 CsI), the problems associated with internal ionisation are no longer present and  
829 the scintillator-coupled EM-CCD is expected to provide further improvements  
830 in spatial resolution and MTF.

## 831 Acknowledgements

832 With thanks to David Burt, Peter Pool and Bill Bruns of e2v technologies.  
833 Also with thanks to all members of the e2v Centre for Electronic Imaging,  
834 past and present, who have offered advice and help in the development of this  
835 project.

## 836 References

- 837 [1] Wernick, M. N. and Aarsvold, J. N., “Emission tomography: the fundamentals  
838 of PET and SPECT”, Academic Press (2004).
- 839 [2] Hall, D. J. and Holland, A., “Photon-counting imaging camera for high-  
840 resolution X-ray and gamma-ray applications”, JINST 6, (2011), C01022.
- 841 [3] Hall, D. J., Holland, A. and Smith, D.R., “Imaging and spectroscopy using a  
842 scintillator-coupled EMCCD”, SPIE 7021, (2008), 70211Z.
- 843 [4] Hall, D. J. and Holland, A., “High resolution X-ray and -ray imaging using  
844 a scintillator-coupled Electron-Multiplying CCD”, Proc. SPIE 7449, (2009),  
845 74491G.
- 846 [5] Hall, D. J., Holland, A. and Smith, D. R., “The use of automatic scale  
847 selection to improve the spatial and spectral resolution of a scintillator-coupled  
848 EMCCD”, Nucl. Instr. Meth. A 604, (2009) 207-210.
- 849 [6] Hall, D. J. (2010) “Exploring the impact of detection physics in X-ray CCD  
850 imagers and spectrometers”. PhD thesis. The Open University.
- 851 [7] Elster, J. and Geitel, H. F., “About the scintillating phosphorence of the  
852 Sitoblende excited by radioactive emanations”, Physikalische Zeitschrift 4,  
853 (1903), 439.
- 854 [8] Rodnyi, P., “Physical processes in inorganic scintillators”, first edition, CRC  
855 Press, Florida, 1997, ISBN: 0-8493-3788-7.
- 856 [9] Schotanus P., Kamermas R., and Dorenbos P., “Scintillation characteristics of  
857 pure and Tl-doped CsI crystals”, IEEE Trans. Nucl. Sci., 37(2) (1990) 177182.
- 858 [10] Bass M., DeCusatis C., Li G., Mahajan V. N., Enoch J., Van Stryland E.,  
859 Optical Society of America, “Handbook of Optics”, third edition, Vol. 4.  
860 McGraw-Hill, 2009, ISBN: 0-0714-9892-3.
- 861 [11] Bill Bruns, e2v, private communication.
- 862 [12] Krause M. O., “Atomic Radiative and Radiationless Yields for K and L Shells”,  
863 J. Phys. Chem. Ref. Data 8, 307 (1979)

- 864 [13] Nagarkar, V.V., Shestakova, I., Gaysinskiy, V., *et al.*, “Fast X-ray/ $\gamma$ -ray imaging  
865 using electron multiplying CCD-based detector”, Nuclear Instruments and  
866 Methods in Physics Research Section A 563(1) (2006) 45-48.
- 867 [14] Miller, B. W., Barber, H. B., Barrett, H. H., Shestakova, I., Singh, B., and  
868 Nagarkar, V. V., “Single-photon spatial and energy resolution of a columnar  
869 CsI(Tl)/EMCCD gamma-camera using maximum-likelihood estimation”, SPIE  
870 6142, (2006), 61421T.
- 871 [15] Pani, R., Pellegrini, R., Cinti, M., N., *et al.*, “Recent advances and future  
872 perspectives of position sensitive PMT”, Nucl. Instr. Meth. A, 213 (2004) 197-  
873 205.
- 874 [16] Pani, R., Pellegrini, R., Cinti, M., N., *et al.*, “A novel compact gamma camera  
875 based on flat panel PMT”, Nucl. Instr. Meth. A, 513 (2003) 36-41.
- 876 [17] Xi, W., Seidel, J., Kakareka, J., *et al.*, “MONICA: a compact, portable dual  
877 gamma camera system for mouse whole-body imaging”, Nucl. Med. Bio. 37  
878 (2010) 245-253.
- 879 [18] Yamamoto, S., “Resolution Improvement Using a Fiber Optic Plate for a Small  
880 Field-of-View NaI(Tl) Gamma Camera”, IEEE Trans. Nucl. Sci., 53(1) (2006)  
881 49.
- 882 [19] Yamamoto, S., Imaizumi, M., Shimosegawa, E., and Hatazawa, J.,  
883 “Development of a compact and high spatial resolution gamma camera system  
884 using LaBr<sub>3</sub>(Ce)”, Nucl. Instr. Meth. A, 622 (2010) 261-269.
- 885 [20] Russo, P., Mettvier, G., Pani, R., Pellegrini, R., Cinti, M., N., and Bennati, P.,  
886 “Imaging performance comparison between a LaBr<sub>3</sub>:Ce scintillator based and  
887 a CdTe semiconductor based photon counting compact gamma camera”, Med.  
888 Phys. 36 (2009) 1298.
- 889 [21] Janesick, J., “Scientific Charge-Coupled Devices”, first edition, *SPIE Press*,  
890 Washington, 2001, ISBN: 0-8194-3698-4.
- 891 [22] Miller, B. W., Barber, H. B., Barrett, H. H., Wilson, D. W., and Liying  
892 C., “A Low-Cost Approach to High-Resolution, Single-Photon Imaging  
893 Using Columnar Scintillators and Image Intensifiers”, IEEE Nuclear Science  
894 Symposium Conference Record 6, (2006), 3540-3545.
- 895 [23] Miller, B., W., Barber, H., B., Barrett, H., H., Chen, L. and Taylor, S., J.,  
896 “Photon-counting gamma camera based on columnar CsI(Tl) optically coupled  
897 to a back-illuminated CCD”, SPIE 6510, (2007), 65100N.
- 898 [24] Jerram, P., Pool, P., Bell, R., Burt, D., Bowring, S., Spencer, S., Hazelwood,  
899 M., Moody, I., Catlett, N., and Heyes, P., “The LLLCCD: Low light imaging  
900 without the need for an intensifier”, Proc. SPIE 4306 (2001) 178-186.
- 901 [25] Mackay, C., D., Tubbs, R., N., Bell, R., Burt, D., Jerram, P., and Moody, I.,  
902 “Sub-electron read noise at MHz pixel rates”, Proc. SPIE 4306, (2001), 289-98.

- 903 [26] Jerram P. A., Pool P. J. , Burt D. J., Bell R. T., Robbins M. S., “Electron  
904 Multiplying CCDs”, SNIC Symposium (Stanford, California), 3-6 April 2006.
- 905 [27] Burkhardt M., and Schwille P., “Electron multiplying CCD based detection for  
906 spatially resolved fluorescence correlation spectroscopy”, Optics Express, 14(12)  
907 (2006) 5013-5020.
- 908 [28] Lees J. E., Bassford D. J., Blake O. E., Blackshaw P. E. and Perkins A. C.,  
909 “A high resolution Small Field Of View (SFOV) gamma camera: a columnar  
910 scintillator coated CCD imager for medical applications”, JINST 6 (2011)  
911 C12033
- 912 [29] Robbins, M., S. and Hadwen, B., J., “The Noise Performance of Electron  
913 Multiplying Charge-Coupled Devices”, IEEE Transactions On Electron Devices  
914 50(5), (2003), 1227-1232.
- 915 [30] J. H. Tutt, D. J. Hall, R. D. Harriss, A. D. Holland, and N. J. Murray, “The  
916 Noise Performance of Electron Multiplying Charge-Coupled Devices at X-rays  
917 energies”, IEEE trans. Elec. Devices, In Press.
- 918 [31] de Vree, G., A., van der Have, F. and Beekman, F., J., “EMCCD-based photon-  
919 counting mini gamma camera with a spatial resolution  $< 100 \mu\text{m}$ ”, IEEE  
920 Nuclear Science Symposium Conference Record 5 (2004) 2724-2728.
- 921 [32] Vree, G. A. d., A. H. Westra, *et al.*, “Photon-Counting Gamma Camera Based  
922 on an Electron-Multiplying CCD”, IEEE Trans. Nucl. Sci. 52(3) (2005) 580-588.
- 923 [33] Beekman, F., J., and de Vree, G., A., “Photon-counting versus an integrating  
924 CCD-based gamma camera: important consequences for spatial resolution”,  
925 Phys. Med. Biol. 50 (2005) N109-N119.
- 926 [34] Heemskerk, J., W., T., Westra, A., H., Linotte, P., M., Ligtoet, K., M.,  
927 Zbijewski, W. and Beekman, F., J., “Frontilluminated versus back-illuminated  
928 photon-counting CCD-based gamma camera: important consequences for  
929 spatial resolution and energy resolution”, Phys. Med. Biol. 52 (2007) N149-  
930 N162.
- 931 [35] Lindeberg, T., “Scale-Space Theory in Computer Vision”, Kluwer Academic  
932 Publishers (1994).
- 933 [36] Korevaar, M., A., N., Heemskerk, J., W., T., Goorden, M., C., and Beekman, F.,  
934 J., “Multi-scale algorithm for improved scintillation detection in a CCD-based  
935 gamma camera”, Phys. Med. Biol. 54 (2009) 831-842.
- 936 [37] R. Pani, M.N. Cinti, R. Pellegrini, P. Bennati, M. Betti, F. Vittorini, M.  
937 Mattioli, G. Trotta, V. Orsolini Cencelli, R. Scafe, F. Navarra, D. Bollini,  
938 G. Baldazzi, G. Moschini, F. de Notaristefani, “LaBr<sub>3</sub>:Ce scintillation gamma  
939 camera prototype for X and gamma ray imaging”, Nuclear Instruments and  
940 Methods in Physics Research A 576 (2007) 1518.
- 941 [38] e2v CCD97 data-sheet, A1A-CCD97BI\_2P\_IMO Issue 3 (2004).

- 942 [39] Hubbell, J.H. and Seltzer, S.M. (2004), Tables of X-Ray Mass Attenuation  
943 Coefficients and Mass Energy-Absorption Coefficients (version 1.4).  
944 Available: <http://physics.nist.gov/xaamdi> (25 January 2011). National  
945 Institute of Standards and Technology, Gaithersburg, MD. Originally published  
946 as NISTIR 5632, National Institute of Standards and Technology, Gaithersburg,  
947 MD (1995).
- 948 [40] Shah, K., S., Glodo, J., Klugerman, M., Higgins., W., M., Gupta, T., and Wong,  
949 P., “High Energy Resolution Scintillation Spectrometers”, IEEE Trans. on Nucl.  
950 Sci., 51(5) (2004) 2395-2399.
- 951 [41] Turchetta R., “Spatial resolution of silicon microstrip detectors”, Nucl. Instr.  
952 and Meth. A, 335 (1993) 44-58.
- 953 [42] Sia, R., Kleinfelder, S., Nagarkar, V., V., “Solid-state photon-counting hybrid  
954 detector array for high-resolution multi-energy X-ray imaging”, Nucl. Instr.  
955 Meth. A, 652 (2011) 470-473.